Journal of Fluorescence, Vol. 9, No. 4, 1999

High-Order Autocorrelation with Imaging Fluorescence Correlation Spectroscopy: Application to IgE on Supported Planar Membranes

Willem Vanden Broek,[1,2] Zhengping Huang,[1,3] and Nancy L. Thompson[1,4]

Received September 15, 1997; accepted June 25, 1999

The use of high-order autocorrelation with imaging fluorescence correlation spectroscopy is described. Fluorescently labeled, antitrinitrophenyl IgE antibodies were specifically bound to substrate-supported planar membranes composed of trinitrophenylaminocaproyldipalmitoylphosphatidylethanolamine and dipalmitoylphosphatidylcholine. The IgE-coated membranes were illuminated with a laser beam that was totally internally reflected at the substrate/solution interface. The evanescently excited fluorescence arising from the membrane-bound IgE was measured with a CCD camera. The images were corrected for background and for the elliptically Gaussian spatial dependence of the evanescent excitation intensity. A series of high-order pixel-to-pixel spatial fluorescence fluctuation autocorrelation functions was calculated from the images. The autocorrelation functions generated multiple independent parameters which were used to characterize the nonuniform spatial distributions of the membrane-bound IgE. These parameters varied with the IgE density and also changed significantly when the IgE-coated membranes were further treated with unlabeled, polyclonal anti-IgE. The high-order autocorrelation functions calculated from images of planar membranes containing fluorescently labeled lipids rather than bound, labeled IgE demonstrated that the spatial nonuniformities were prominent only in the presence of IgE. Images of fluorescent beads were used to demonstrate the principles and the methods.

KEY WORDS: Fluorescence fluctuation; photon correlation; image analysis; total internal reflection; evanescent illumination; receptor clustering.

INTRODUCTION

Molecular events at cell surfaces are central to signal transduction and subsequent cellular response. In many cases, cellular response is initiated or mediated by receptor dimers or higher-order oligomers [1–6]. Receptor oligomerization has been implicated or confirmed in a large variety of signal transduction processes, including those mediated by epidermal growth factor [7–10], fibroblast growth factor [11,12], granulocyte-colony stimulating factor [13], immunoglobulins [14–16], fibronectin [17], insulin [18], interleukins [19], and erythropoietin [20]. However, few experimental methods exist for examining the oligomerization of cell-surface receptors.

One approach that holds promise as a method for characterizing receptor dimerization or higher order oligomerization is fluorescence correlation spectroscopy (FCS) [21]. In conventional FCS, fluorescent molecules

[1] Department of Chemistry, University of North Carolina, Chapel Hill, North Carolina 27599-3290.
[2] Present address: MAIK Nauka, Box 54, c/o Post International, 666 Fifth Avenue, Suite 572, New York, New York 10103.
[3] Present address: Biology and Biotechnology Research Program, Lawrence Livermore National Laboratory, P.O. Box 808, MS L-452, 7000 East Avenue, Livermore, California 94550.
[4] To whom correspondence should be addressed at Department of Chemistry, Campus Box 3290, University of North Carolina, Chapel Hill, North Carolina 27599-3290. e-mail: nlt@unc.edu

1053-0509/99/1200-0313$16.00/0

move in solution through a small illuminated region, generating temporal fluctuations in the fluorescence emitted from the region. The magnitude of the normalized fluorescence fluctuation autocorrelation function depends in a nonlinear manner on the fluorescence yields of the different species and is therefore sensitive to molecular clustering [22,23]. Conventional FCS has not been extensively applied to model or natural membranes. A major limitation is that significant fractions of the fluorescent molecules are often immobile or only slowly mobile. In this case, focused laser beams generate local bleached regions and subsequent small mechanical fluctuations cause fluorescence fluctuations that are not related to molecular number fluctuations and receptor oligomerization. Also, the diffusion process must be relatively fast in conventional FCS so that a lengthy enough sampling of the fluorescence fluctuations can be obtained in an experimentally reasonable time.

Scanning fluorescence correlation spectroscopy (S-FCS) addresses these difficulties. In S-FCS, the sample is translated through a focused laser beam, or a focused laser beam is translated through the sample, and fluorescence fluctuations are measured as a function of position rather than time [24–28]. This method often employs a scanning confocal laser microscope [29–31]. In a somewhat different approach, called imaging FCS (I-FCS) [32–38], the pixel-to-pixel fluorescence fluctuations from a single fluorescence image, obtained with a CCD camera, are spatially autocorrelated. Two primary advantages of I-FCS compared to S-FCS are that a large number of data points, rather than one, are collected per sample time and that the requirement for fast diffusion, sample translation, or optical motion is eliminated.

In conventional FCS, for an ergodic and monodisperse sample, the extrapolated magnitude of the normalized fluorescence fluctuation autocorrelation function is proportional to the inverse of the average number of fluorescent molecules in the sample volume. The magnitude can yield a measure of the fluorescent molecule number density provided that the proportionality constant, which is related to instrumental factors, has been calibrated with samples of known concentration [21]. However, for polydisperse samples, the magnitude of the normalized fluorescence fluctuation autocorrelation function depends on the number densities of the different fluorescent species as well as their relative fluorescence intensities [23]. One is confronted with the difficulty of having only one measured number and more than one unknown. The rate and shape of the decay of the fluorescence fluctuation autocorrelation function contain information about the temporal behavior of the different fluorescent species, but resolving the monotonically decaying autocorrelation function into the contributing characteristic rates and their amplitudes can be difficult [39]. If two species are present representing monomers and dimers, the characteristic rates associated with translational diffusion differ by a factor of only approximately $2^{1/3}$. For all but very high signal-to-noise ratios, resolving decay components with such small differences in characteristic times is not straightforward. One method of overcoming this difficulty is to calculate, from the same time record of fluorescence, a series of high-order autocorrelation functions. For a polydisperse sample, the magnitudes of the higher-order autocorrelation functions contain independent information about the number densities and relative fluorescence yields of the different fluorescent species [40–44].

The work described here presents the concept of using high-order autocorrelation with I-FCS. High-order spatial fluorescence fluctuation autocorrelation functions are defined as

$$G_{mn}(\rho) = \frac{\langle \delta F^m(r)\, \delta F^n(r+\rho)\rangle - \langle \delta F^m\rangle\langle \delta F^n\rangle}{\langle F\rangle^{m+n}} \qquad (1)$$

where the brackets indicate a spatial average; $F(r)$ is the fluorescence intensity at position r, corrected for background and for the spatial dependence of the excitation intensity; $\delta F(r) = F(r) - \langle F\rangle$; and $m,n > 0$ are integers. The offset has been defined so that $G_{mn}(\infty) = 0$ for samples without long-range spatial correlations, and the autocorrelation functions have been normalized so that they are unitless. High-order fluorescence fluctuation autocorrelation has previously been developed in combination with temporal FCS as a method for detecting and characterizing molecular oligomers in solution [22,40–44] but has not previously been combined with I-FCS. The method is demonstrated on fluorescent beads and applied to tetramethylrhodamine-labeled, antitrinitrophenyl IgE specifically bound to substrate-supported planar membranes composed of trinitrophenylaminocaproylphosphatidylethanolamine and dipalmitoylphosphatidylcholine.

MATERIALS AND METHODS

Fluorescent Beads. Suspensions of fluorescein-labeled microbeads were obtained commercially (Polysciences, Inc., Warrington, PA). Bead suspensions were dialyzed against phosphate-buffered saline (PBS; 0.05 *M* sodium phosphate, 0.15 *M* sodium chloride, 0.01%

sodium azide, pH 7.4) and diluted 10-fold with PBS. The bead diameters were 1 μm or 50 nm.

Antibodies. Monoclonal antitrinitrophenyl (TNP) IgE antibodies were purified from supernatants of the hybridoma TIB142 (American Type Culture Collection, Rockville, MD) by affinity chromatography with dinitrophenyl-conjugated human serum albumin [45]. Polyclonal sheep anti-mouse IgE antibodies were obtained commercially (Calbiochem, La Jolla, CA). The IgE antibodies were labeled with tetramethylrhodamine isothiocyanate (denoted R-IgE) (Molecular Probes, Inc., Junction City, OR) as described previously [46]. Antibody concentrations were determined spectrophotometrically [34,46]. Antibodies were passed through 0.2-μm filters and clarified (100,000*g*, 30 min) no more than 10 h prior to application to planar membranes.

Phospholipid Vesicles. 1,2-Dipalmitoyl-*sn*-glycero-3-phosphocholine (DPPC), 1,2-dipalmitoyl-*sn*-glycero-3-phosphoethanolamine-*N*-[6[(2,4,6-trinitrophenyl)-amino]caproyl] (TNP–cap-DPPE), and 1,2-dipalmitoyl-*sn*-glycero-3-phosphoethanolamine-*N*-(7-nitro-2-1,3-benzoxadiazol-4-yl) (NBD–DPPE) were obtained commercially (Avanti Polar Lipids, Birmingham, AL) and used without further purification. Small unilamellar vesicles were prepared, with the total phospholipid concentration equal to 2 m*M*, by probe sonication [47]. The vesicle composition was TNP–cap-DPPE/DPPC (25/75, mol/mol) or TNP–cap-DPPE/DPPC/NBD–DPPE (25/70/5, mol/mol/mol).

Sample Chambers. Glass microscope coverslips (No. 0; 24 × 60 mm) were attached to aluminum supports containing apertures (0.8 × 0.8 in.) with Sylgard 184 silicone elastomer (Dow Corning Corp., Midland, MI). Fused silica slides (1 in. × 1.2 in. × 1 mm; Quartz Scientific, Fairport Harbor, OH) and polylysine-coated glass slides (1 in. × 1.2 in. × 1 mm; Polysciences, Inc., Warrington, PA) were obtained commercially. Aluminum supports and fused silica slides were cleaned by boiling with Cleaning Solution (ICN, Costa Mesa, CA), bath sonicating, and rinsing extensively with deionized water. Polylysine-coated slides were cleaned by rinsing with ethanol and deionized water. Fused silica slides and polylysine-coated slides were attached to aluminum supports with two strips of single-coated Kapton polyimide adhesive film (0.001 in.; Saunders Engineering Corp., Raleigh, NC) and aluminum clips.

Sample Preparation. Mounted polylysine-coated slides were treated with 100-μl bead suspensions for 30 min and then rinsed with 1 ml PBS. Mounted fused silica slides were treated with vesicle suspensions to form substrate-supported planar membranes [47]. Supported membranes were treated with 250 μl PBS containing various concentrations of R-IgE for 30 min and then washed with 1 ml PBS. Membranes were treated with 0.062, 0.17, 0.38, or 1 μM R-IgE; these concentrations populated the surface with specifically bound R-IgE to 20, 40, 60, or 80% of the maximum density, respectively [34]. Some samples treated with 0.38 μ*M* R-IgE were further treated with 250 μl of 0.1 mg/ml unlabeled, polyclonal anti-IgE in PBS for 30 min and rinsed with 1 ml PBS.

Fluorescence Microscopy. The fluorescence microscope was composed of an argon ion laser (Coherent Innova 90-6), an inverted optical microscope (Zeiss Axiovert), and a slow-scan cooled CCD (Photometrics KAF-1400). The laser beam was directed through a focusing lens (focal length, 100 mm) and a cubic fused silica prism [(1.5 cm)^3] and totally internally reflected at the interface of the fused silica or polylysine-coated slides and the solution [48]. Evanescently excited fluorescence was collected through a microscope objective (Nikon; oil-immersion, 60 ×, NA 1.4) and directed through a dichroic mirror and barrier filter to the CCD. Previous work has demonstrated that illumination by internal reflection generates less background light than epiillumination [34]. Images were acquired with the following conditions: wavelength, 488.0 nm for fluorescein-coated beads or fluorescent lipids and 514.5 nm for R-IgE; angle of incidence on the substrate–solution interface, ≈ 75°; laser power, 5–20 mW; size of illuminated area, ≈30 × 80 μm; camera exposure time, 100–500 ms; and pixel area at the sample plane, (0.11 μm)^2. For each sample type, 4–19 images were acquired from two to five independently prepared samples.

Calculation of Fluorescence Fluctuation Autocorrelation Functions. Images were corrected for background by subtracting the dark counts obtained as bias images. Subimages were selected from the background-corrected images as rectangular areas from well within the illuminated regions and were typically 26 × 68 μm. Subimages were corrected for the approximate elliptically Gaussian shape of the evanescent intensity[5] as described previously [34]. The $G_{mn}(\rho)$, for $\rho = k\Delta$, where Δ is the dimension of a single pixel (0.11 μm), were calculated from corrected subimages according to Eq. (1) and

$$\langle F \rangle = \frac{1}{MN} \sum_{i=1}^{M} \sum_{j=1}^{N} F(i,j),$$
$$\langle \delta F^m \rangle = \frac{1}{MN} \sum_{i=1}^{M} \sum_{j=1}^{N} [F(i,j) - \langle F \rangle]^m \quad (2)$$

[5] The smoothing routine is not completely rigorous and awaits future refinement and testing.

$$\langle \delta F^m(r)\delta F^n(r+\rho)\rangle = \frac{1}{(M-k)N + (N-k)M} \cdot \{ \sum_{i=1}^{M-k} \sum_{j=1}^{N} [F(i,j) - \langle F\rangle]^m [F(i+k,j) - \langle F\rangle]^n - \sum_{i=1}^{M-k} \sum_{j=1}^{N-k} [F(i,j) - \langle F\rangle]^m [F(i,j+k) - \langle F\rangle]^n \} \quad (3)$$

where i and j are the row and column numbers; N and M are the numbers of rows and columns in the subimage, respectively; and $F(i,j)$ is the corrected intensity at pixel (i,j). $G_{mn}(k\Delta)$ were calculated for $k = 0$ to 49 and for $2 \leq m + n \leq 6$. The experimental values of $\langle F\rangle$ were always close to unity.

In conventional (temporal) FCS, fluorescence fluctuation autocorrelation functions are corrected for background by using a factor found from the average signal intensity and the average background intensity [21,23]. In this work, the background (obtained as a bias image) is subtracted before calculation of autocorrelation functions, and the multiplicative factor is not required. In addition, although contributions from photon counting statistics (shot noise) are present in $G_{11}(\rho)$ only in the first channel ($\rho = 0$), they are in general present in high-order autocorrelation functions in all channels ($\rho > 0$) [22,23,41]. Using previously derived expressions for these effects, it was determined that the corrections were small (usually 0.1% to 5%) for the images analyzed in this work. Therefore, these postcalculation corrections to the $G_{mn}(\rho)$ were not carried out.

RESULTS

Fluorescence Images and Their Spatial Autocorrelation Functions. Figures 1a and b show typical images of fluorescent beads with 1-μm and 50-nm diameters, respectively. Images of membranes containing 5 mol % NBD–DPPE appeared uniform (Fig. 1c). The broad elliptical shape was due to the spatial dependence of the illumination intensity. Figure 1d shows a typical fluorescence image of TNP–cap-DPPE/DPPC planar membranes containing bound R-IgE at 20% of the saturating density. As shown, the spatial distribution of R-IgE was not uniform. The nonuniformities appeared to be several pixels wide and therefore of sizes approximately equal to optical resolution. The images for 80% saturation (Fig. 1e) showed much larger nonuniformities and higher contrasts in intensity between dark and bright regions. Some of the R-IgE samples with 60% surface saturation were treated with 0.1 mg/ml unlabeled anti-IgE. Images of these samples (Fig. 1f) indicated that, as expected, the anti-IgE induced larger and brighter clusters. Experimental $G_{mn}(\rho)$ were calculated from fluorescence images as described above (Fig. 2). The autocorrelation functions varied considerably in both magnitude and shape for different sample types and different values of m and n.

Autocorrelation Function Magnitudes. The values of $G_{mn}(0)$ are related to spatial nonuniformities in the fluorescence images. However, these values also contain contributions from the statistics of photon counting and from residual noise related to subtraction of bias images as background. For our purposes, the values $G_{mn}(0)$ as extrapolated from values of $\rho > 0$, denoted here G_{mn}, were determined. The G_{mn} were found by assuming that the first four points of $G_{mn}(\rho)$ are adequately described by a third-order polynomial in ρ^2. For this functional form, the four polynomial constants can be determined exactly from $G_{mn}(\rho)$ for the first four nonzero values of ρ; one constant equals G_{mn}.

In the simplest case where the background-corrected fluorescence, normalized by the excitation intensity, is proportional to the concentration of fluorescent molecules, the G_{mn} are related to spatial nonuniformities in the concentrations of fluorescent molecules as

$$G_{mn} = \frac{\langle \delta C^{m+n}\rangle - \langle \delta C^m\rangle\langle \delta C^n\rangle}{\langle C\rangle^{m+n}} \quad (4)$$

where $C(r)$ is the concentration of fluorescent molecules and $\delta C(r) = C(r) - \langle C\rangle$ is the fluorescence and concentration fluctuation at position r. With $\langle \delta C\rangle = 0$, Eq. (4) implies that

$$\begin{aligned} G_{mn} &= G_{nm} \\ G_{13} &= G_{22} + G_{11}^2 \\ G_{14} &= G_{23} + G_{11}G_{12} \\ G_{15} &= G_{24} + G_{11}G_{13} = G_{33} + G_{12}^2 \end{aligned} \quad (5)$$

The complete data set was examined to verify the expressions in Eqs. (5).[6]

It is instructive to define parameters

$$S_p = \frac{\langle \delta C^p\rangle}{\langle C\rangle^p}, \qquad B_p = \frac{\langle C^p\rangle}{\langle C\rangle^p} \quad (6)$$

[6] This analysis showed that these equations were correct to within 0.5–1.5 % for cases in which $S_p > 0.1$ (fluorescent beads, membranes at 80% R-IgE saturation, and membranes containing anti-IgE). For samples 20–60% saturated with R-IgE, G_{12} differed from G_{21} by 3–16%, G_{13} differed from G_{31} by 11–14%, and G_{13} differed from $G_{22} + G_{11}^2$ by 16–21%. The left and right sides of the other seven expressions in Eq. (5) were equivalent for these samples, on the average, only within a factor of two. Even larger percentage differences were observed for the samples containing fluorescent lipids in which the values of S_p were very low.

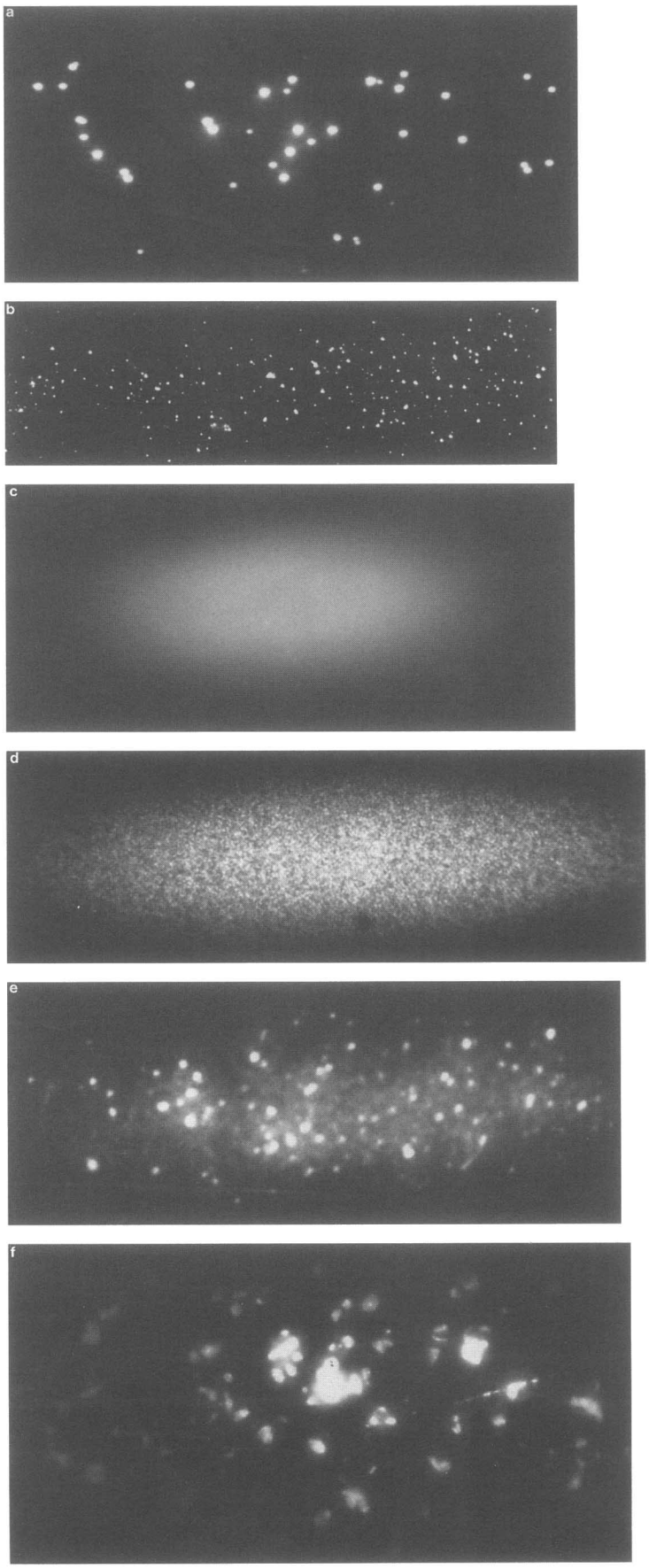

Fig. 1. Fluorescence images. Images of planar samples of different compositions are visually distinctive: (a) polylysine-coated glass with adsorbed 1-μm flourescence beads; (b) polylysine-coated glass with adsorbed 50-nm fluorescence beads; (c) TNP–cap-DPPE/DPPC/NBD–DPPE planar membrane; (d) TNP–cap-DPPE/DPPC planar membrane containing a density of R-IgE corresponding to 20% surface saturation; (e) TNP–cap-DPPE/DPPC planar membrane containing a density of R-IgE corresponding to 80% surface saturation; (f) TNP–cap-DPPE/DPPC planar membrane containing a density of R-IgE corresponding to 60% surface saturation and further treated with unlabeled, polyclonal anti-IgE. The image sizes (μm) are (a) 57 × 117, (b) 33 × 112, (c) 51 × 116, (d) 46 × 136, (e) 50 × 124, and (f) 66 × 126.

These parameters are found from the G_{mn} by the following sequential calculations [22,23,40]:

$$S_2 = G_{11}$$

$$S_3 = \frac{1}{2}[G_{12} + G_{21}]$$

$$S_4 = \frac{1}{3}[G_{13} + G_{31} + G_{22} + S_2^2] \quad (7)$$

$$S_5 = \frac{1}{4}[G_{14} + G_{41} + G_{23} + G_{32} + 2S_2S_3]$$

$$S_6 = \frac{1}{5}[G_{15} + G_{51} + G_{24} + G_{42} + G_{33} + 2S_2S_4 + S_3^2]$$

and

$$B_2 = S_2 + 1$$

$$B_3 = S_3 + 3S_2 + 1$$

$$B_4 = S_4 + 4S_3 + 6S_2 + 1 \quad (8)$$

$$B_5 = S_5 + 5S_4 + 10S_3 + 10S_2 + 1$$

$$B_6 = S_6 + 6S_5 + 15S_4 + 20S_3 + 15S_2 + 1$$

For a uniform image, $\delta C(r) = 0$, $S_p = 0$, and $B_p = 1$. Thus, values of $B_p > 1$ indicate spatial nonuniformities (Fig. 3). The values of $B_2 - 1$ calculated from images of fluorescent beads were large (1.5 and 0.4 for 1-μm and 50-nm beads, respectively), and the $B_2 - 1$ were much smaller ($\approx 10^{-3}$) for planar membranes containing fluorescent lipids, as expected. $B_2 - 1$ ranged from 0.007 to 0.14 for planar membranes containing different densities of bound R-IgE. When membranes 60% saturated with R-IgE were treated with anti-IgE, $B_2 - 1$ increased to 0.5. The B_p increased monotonically with p for all image types. In general, the different sample types exhibit significant differences both in the magnitudes of B_p and in the dependence of these parameters on the index p. This result demonstrates that the parameters B_p contain distinct information about the different patterns of nonuniformities on the samples.

Autocorrelation Function Correlation Distances. Correlation distances, denoted R_{mn}, were defined for the autocorrelation functions as the distances at which the $G_{mn}(\rho)$ had decayed by factors of two (Fig. 4). Values of R_{mn} were obtained by linear interpolation between the two values of $G_{mn}(\rho)$ which were higher and lower than $^1/_2\ G_{mn}$.[7] In cases where both R_{mn} and R_{mn} were obtained, the correlation distances were averaged and denoted R_{mn}, where $m < n$. The correlation distance R_{11} for 1-μm beads agreed well with the known bead diameter, whereas the correlation distance for 50-nm beads was significantly higher (by a factor of ≈10) than the known bead diameter. The latter result is attributed to the optical transfer function of the microscope. The correlation distances R_{11} for planar membranes 20, 40, and 60% saturated with R-IgE were equivalent within experimental uncertainty to the correlation distance for 50-nm beads, indicating that the average IgE cluster size in these samples was smaller than or approximately equal to optical resolution. Significantly higher values of R_{11} were found for membranes 80% saturated with R-IgE or treated with anti-IgE. The correlation distances R_{mn} decreased with the index n (for constant m) and with the index m (for constant n).

Models for Surface Inhomogeneities. As a model, we assume that the surface is populated by discrete regions with different concentrations of fluorescent molecules and therefore of different fluorescence intensities. Each new constant B_p provides one new, independent parameter for characterizing surface inhomogeneities. To explore this type of model, the number of region types, denoted q, is increased as the number of B_p values, denoted s, is increased. From Eq. (6),

$$B_p = \frac{\sum_{i=1}^{q} a_{si} C_{si}^p}{\left[\sum_{i=1}^{q} a_{si} C_{si}\right]^p} = \frac{\sum_{i=1}^{q} a_{si}\, b_{si}^p}{\left[\sum_{i=1}^{q} a_{si} b_{si}\right]^p} \quad (9)$$

where C_{si} is the concentration of molecules in regions of the ith type, $b_{si} = C_{si}/C_{s1}$ are the relative concentrations, a_{si} are the fractions of the surface that are occupied by regions of the ith type, q is the number of region types, and

$$\sum_{i=1}^{q} a_{si} = 1 \quad (10)$$

Relationships among the a_{si}, b_{si}, and B_p can be found algebraically (Appendix).

From the lowest-order autocorrelation function, $G_{11}(\rho)$, one obtains only one number (B_2) that is related

[7] For images of fluorescent beads, the signal-to-noise ratios of the $G_{mn}(\rho)$ were high, so that all of the R_{mn} could be determined by interpolation. For membranes treated with anti-IgE, the R_{mn} could be determined in this manner for all cases except $m = n = 3$. For some images of membranes 80% saturated with R-IgE and some values of m and n, the signal-to-noise ratios were not high enough for interpolation; these cases (6% overall) were excluded. For membranes 20, 40, and 60% saturated with R-IgE, a significant fraction of the G_{mn} was of low enough magnitude so that the R_{mn} could not be determined. In addition, interpolation gave unrealistically high values in some cases because the $G_{mn}(\rho)$ did not approach zero, relative to G_{mn}, for large ρ. For these three sample types, average correlation distances were calculated for given values of m and n only if more than 75% of the R_{mn} from a given image type could be determined. Correlation distances were not calculated for membranes containing fluorescent lipids.

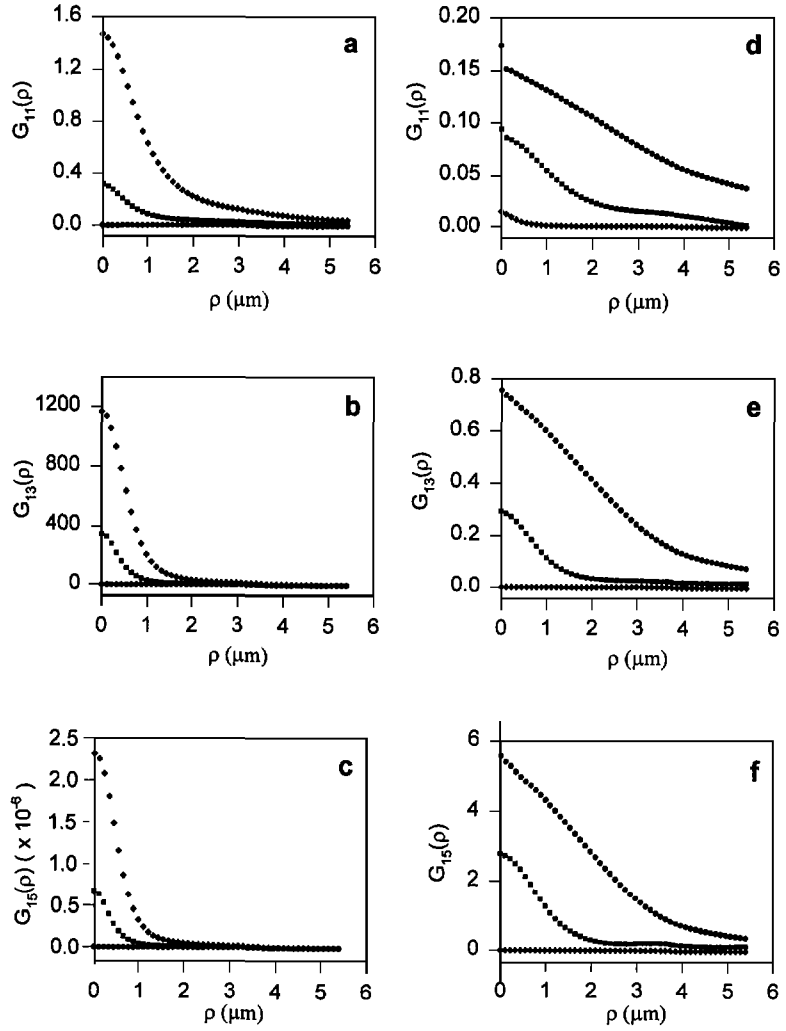

Fig. 2. High-order autocorrelation functions. Functions $G_{mn}(\rho)$ were calculated from sub-images that had been corrected for background and for the spatially nonuniform illumination as described in the text. Representative calculations are shown. Experimentally calculated values of (a, d) $G_{11}(\rho)$, (b, e) $G_{13}(\rho)$, and (c, f) $G_{15}(\rho)$ are compared. In a–c, the samples were (♦) 1-μm fluorescent beads on polylysine-coated fused silica, (■) 50-nm fluorescent beads on polylysine-coated fused silica, or (●) TNP–cap-DPPE/DPPC/NBD–DPPE planar membranes. In d–f, the samples were TNP–cap-DPPE/DPPC planar membranes (♦) 20% saturated with R-IgE, (■) 80% saturated with R-IgE, and (●) 60% saturated with R-IgE and further treated with anti-IgE.

to molecular clustering ($s = 1$). In this case, the simplest model is one in which the surface is assumed to be populated with a single type of cluster ($q = 2$, $b_{11} = 1$, and $b_{12} = 0$). The values of a_{11} and a_{12} are found from Eq. (A1) and are shown in Table I for the different sample types. For images of fluorescent lipids and membranes 20–60% saturated with R-IgE, this analysis implies that the majority (≈99%) of the pixels have approximately equivalent intensities. For membranes 80% saturated with R-IgE, membranes containing anti-IgE, and for images of fluorescent beads, nonnegligible amounts of pixels (7–58%) have zero intensities relative to the other pixels. This initial analysis, based only on $G_{11}(\rho)$, reflects the qualitative observation that the rank order of image contrast is 1-μm beads > anti-IgE > 50-nm beads > 80% R-IgE > 60% R-IgE ≈ 40% R-IgE ≈ 20% R-IgE > fluorescent lipids (Fig. 1).

From the two lowest-order autocorrelation functions, one obtains two numbers (B_2 and B_3) that are related to molecular clustering ($s = 2$). In this case, the simplest

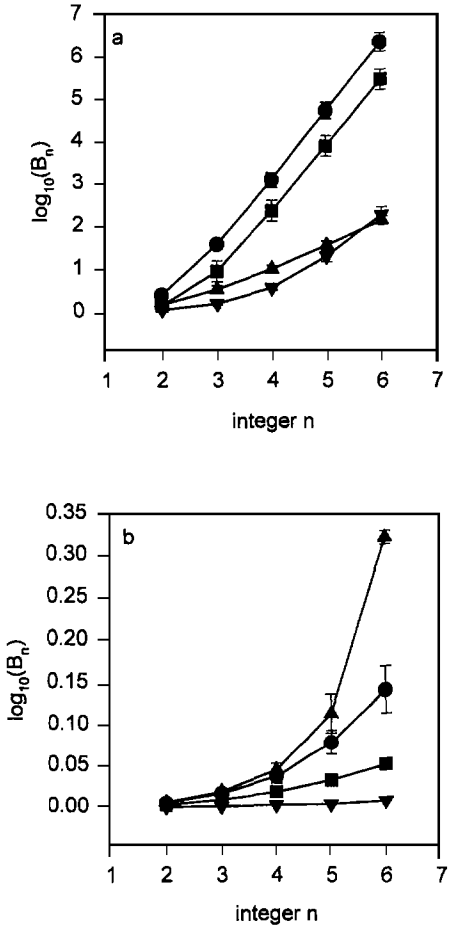

Fig. 3. Experimental values of B_p. Extrapolated values of $G_{mn}(0) = G_{mn}$ were determined for each image from the values of $G_{mn}(k\Delta)$, for $k = 1$ to 4, as described in the text. The values of S_p were determined from the G_{mn} according to Eqs. (7) and the values of B_p were then determined from the values of S_p using Eqs. (8). B_p values are shown for (a; ●) 1-μm beads, (a; ■) 50-nm beads, (a; ▲) membranes treated with R-IgE and anti-IgE, (a; ▼) membranes 80% saturated with R-IgE, (b; ●) membranes 60% saturated with R-IgE, (b; ■) membranes 40% saturated with R-IgE, (b; ▲) membranes 20% saturated with R-IgE, and (b; ▼) membranes containing NBD-DPPE. Uncertainties are standard deviations of the means and are shown only when larger than the point size.

model is one in which the surface is assumed to be populated by a single type of cluster against a nonzero background. There are two types of regions, but they may be characterized so that they both contain nonzero concentrations of fluorescent molecules ($q = 2$, $b_{21} = 1$, $b_{22} > 1$). The values of a_{21}, a_{22}, and b_{22} are found from Eqs. (A2) and are shown in Table I for the different sample types. For the high-contrast samples (fluorescent beads, 80% R-IgE, anti-IgE), the majority of the pixels (≥90%) have low intensities ($b_{21} = 1$) and a minority (≤10%) of the pixels have higher intensities ($b_{22} \approx 3$–21). The 20, 40, and 60% R-IgE samples show significant (24–29%) populations of pixels with relative intensities only slightly higher than one ($b_{22} \approx 1.2$–1.4). The two populations for fluorescent lipids have approximately equivalent intensities ($b_{22} < 1.1$).

For B_2, B_3, and B_4 ($s = 3$), the surface is assumed to be populated by three types of regions. Two region types correspond to different cluster types and one region is a zero-intensity background ($q = 3$, $b_{31} = 1$, $b_{32} > 1$, $b_{33} = 0$). The values of a_{31}, a_{32}, a_{33}, and b_{32} are found from Eqs. A3 (Table I). The results are similar to those found for the two-parameter model. The low intensity pixels are split between the those having relative intensities of zero and one ($a_{31} + a_{33} \approx a_{21}$). The values of a_{32} and b_{32} are similar to the values of a_{22} and b_{22} found in the two-parameter model.

For B_2, B_3, B_4, and B_5 ($s = 4$), the surface is assumed to be populated by three types of regions, all of which contain nonzero intensities ($q = 3$, $b_{41} = 1$, $b_{42} > 1$, $b_{43} > 1$). The values of a_{41}, a_{42}, a_{43}, b_{42}, and b_{43} are found from Eqs. (A4)–(A6) (Table I). For the high-contrast samples (fluorescent beads, 80% R-IgE, anti-IgE), the majority of the pixels have equivalent intensities ($b_{41} = 1$) and a minority of the pixels have higher intensities (b_{42}, $b_{43} > 1$). Compared to the two-parameter model, the fractions of pixels having high intensities are higher ($a_{42} + a_{43} > a_{22}$). In addition, the values of b_{42} are lower, and the values of b_{43} are higher, than the values of b_{22}. For the 20, 40, and 60% R-IgE samples, $b_{42} \approx 1$. In these cases, the fractions of pixels with a high intensity (a_{43}) are much lower than the fractions for the three-parameter (a_{32}) and two-parameter (a_{22}) models. This result suggests that increasing the number of parameters by using high order autocorrelation provides significant new information. The majority of the pixels for images of fluorescent lipids ($a_{41} + a_{42}$) have approximately equivalent intensities ($b_{42} = 1.07$), and very small fractions have significantly lower intensities.

For B_2, B_3, B_4, B_5, and B_6 ($s = 5$), the surface is populated by four types of regions, three of which contain nonzero intensities and one which corresponds to a zero background ($q = 4$, $b_{51} = 1$, $b_{52} > 1$, $b_{53} > 1$, $b_{54} = 0$). As calculated using Eqs. (A7)–(A9) and shown in Table I, increasing the analysis from four to five parameters is similar to increasing from two to three parameters in that the low-intensity pixels are split between those having relative intensities of zero and one ($a_{51} + a_{54} \approx a_{41}$). The values of a_{52}, a_{53}, b_{52}, and b_{53} are similar to the values of a_{42}, a_{43}, b_{42}, and b_{43}, respectively.

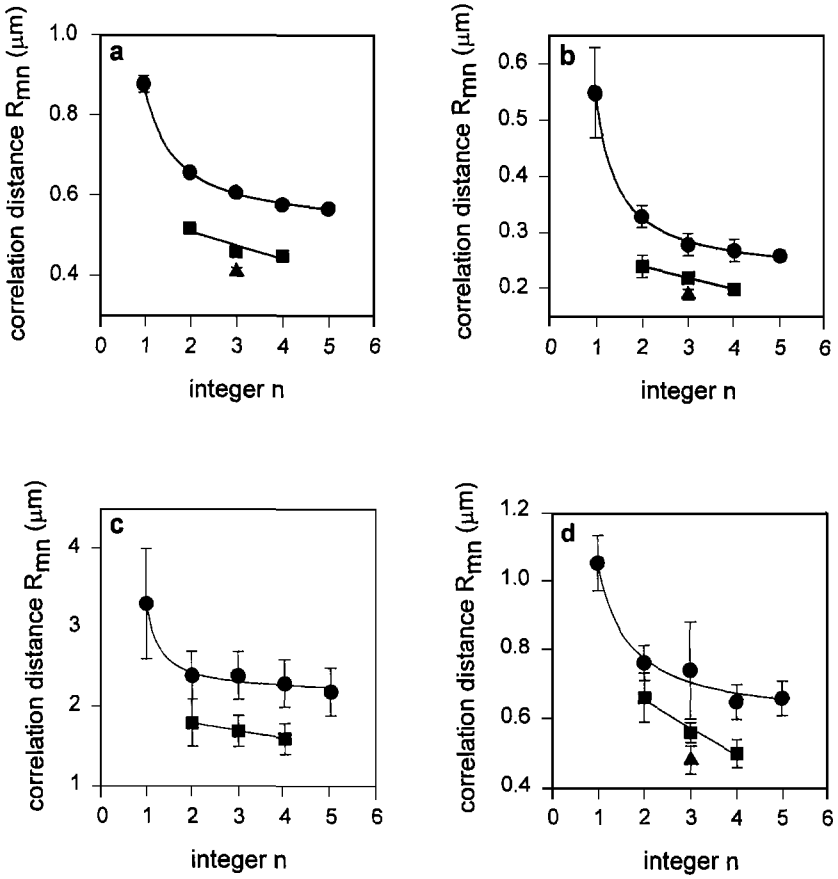

Fig. 4. Correlation distances R_{mn}. Correlation distances were determined as described in the text: (a) 1-μm beads; (b) 50-nm beads; (c) TNP–cap-DPPE/DPPC membranes containing bound R-IgE and anti-IgE; (d) TNP–cap-DPPE/DPPC membranes 80% saturated with R-IgE. Symbols denote (●)R_{1n}, (■) R_{2n}, and (▲) R_{33}. Uncertainties are standard deviations of the means and are shown only when larger than the point size. Correlation distances for membranes 20, 40, and 60% saturated with R-IgE ranged between the distances for 50-nm beads (b) and membranes 80% saturated with R-IgE (d).

For spatially distinct, homogeneous clusters, the cluster density η can be estimated as the ratio of the fractional area occupied by clusters and the approximate cluster size, i.e.,

$$\eta = \frac{a_{42} + a_{43}}{\pi R_{11}^2}, \qquad \eta' = \frac{a_{43}}{\pi R_{11}^2} \tag{11}$$

where η is for the three high-contrast samples and η' is for membranes 20–80% saturated with R-IgE. For 1-μm fluorescent beads, $\eta = 0.0065/\mu m^2$; and for 50-nm fluorescent beads, $\eta = 0.011/\mu m^2$. For membranes coated with R-IgE, the calculated values are $\eta = 0.0058/\mu m^2$ (anti-IgE), $\eta' = 0.0011/\mu m^2$ (80%), $\eta' = 0.035/\mu m^2$ (60%), $\eta' = 0.035/\mu m^2$ (40%), and $\eta' = 0.030/\mu m^2$ (20%). These values agree qualitatively with visual inspection of the images.

DISCUSSION

In previous work [34], we demonstrated the feasibility of using a CCD detector with spatial fluorescence fluctuation autocorrelation (I-FCS) for detecting and characterizing molecular clusters in model cell membranes. An advantage of I-FCS compared to conventional FCS is that a large number of data points, rather than one, may be collected per sample time. In addition, I-FCS does not require fast diffusion, sample translation, moving optical components, or acquisition of consecutive images. As a result of the microscope's optical transfer function, appreciable spatial correlations persist for several pixels even when fluorescent entities are smaller than optical resolution. Therefore, I-FCS has potential

Table I. Models for Surface Inhomogeneities[a]

Parameter s	1		2		3			4			5			
Region types q	2		2		3			3			4			
Integer i	1	2	1	2	1	2	3	1	2	3	1	2	3	4
1-μm beads														
a_{si}	0.42	0.58	0.994	0.006	0.69	0.0024	0.30	0.984	0.015	7×10^{-4}	0.84	0.007	4.3×10^{-4}	0.15
b_{si}	1	0	1	21	1	18	0	1	11	38	1	13	33	0
50-nm beads														
a_{si}	0.81	0.19	0.998	0.0025	0.90	6×10^{-4}	0.10	0.989	0.010	1.7×10^{-4}	0.95	0.003	1.0×10^{-4}	0.05
b_{si}	1	0	1	13	1	17	0	1	6	26	1	9	25	0
Anti-IgE														
a_{si}	0.7	0.3	0.90	0.10	0.82	0.06	0.12	0.80	0.17	0.03	0.81	0.11	0.017	0.06
b_{si}	1	0	1	4.4	1	3.7	0	1	3.2	7	1	3.1	5.7	0
80% R-Ige														
a_{si}	0.93	0.07	0.95	0.05	0.955	0.026	0.019	0.77	0.22	0.0039	0.86	0.13	0.0022	0.006
b_{si}	1	0	1	3.0	1	3.8	0	1	1.8	5	1	2.3	6	0
60% R-IgE														
a_{si}	0.989	0.011	0.76	0.24	0.82	0.18	7×10^{-4}	0.64	0.34	0.016	0.64	0.34	0.011	4×10^{-5}
b_{si}	1	0	1	1.30	1	1.34	0	1	1.07	1.7	1	1.04	1.64	0
40% R-IgE														
a_{si}	0.993	0.0070	0.71	0.29	0.78	0.22	2.6×10^{-4}	0.69	0.28	0.036	0.60	0.38	0.021	2×10^{-5}
b_{si}	1	0	1	1.20	1	1.22	0	1	0.95	1.3	1	0.97	1.37	0
20% R-IgE														
a_{si}	0.987	0.013	0.71	0.29	0.77	0.23	0.002	0.59	0.40	0.02	0.68	0.31	0.008	0.0012
b_{si}	1	0	1	1.37	1	1.6	0	1	0.90	2.2	1	1.2	2.7	0
NBD–DPPE														
a_{si}	0.999	0.0011	0.40	0.60	0.59	0.41	4.9×10^{-5}	0.75	0.25	0.003	0.74	0.25	0.004	1.8×10^{-5}
b_{si}	1	0	1	1.09	1	1.09	0	1	1.07	0.6	1	1.02	1.0	0

[a] For each model, the parameter s denotes the number of B_p values used and the parameter q denotes the numbers of region types. The parameters a_{si} are the fractions of the surface covered by different region types and the parameters b_{si} are the relative fluorescence intensities of each region type. Values of b_{si} equal to 0 or 1 are fixed by the model and are not free parameters. Uncertainties were calculated for each value of a_{si} and unfixed value of b_{si} as standard deviations of the means and are denoted by the last digit (e.g., 0.58 was derived from 0.58 ± 0.03, and 0.994 was derived from 0.994 ± 0.001).

applicability to molecular oligomers (such as receptor dimers).

In the work described here, we explored the possibility of using high-order autocorrelation with I-FCS. A variety of sample types was examined, including TNP–cap-DPPE/DPPC planar membranes containing different densities of specifically bound R-IgE, membranes containing bound R-IgE that was cross-linked with unlabeled, polyclonal anti-IgE, membranes containing fluorescent lipids, and two sizes of fluorescent beads. High-order spatial fluorescence fluctuation autocorrelation functions could be determined for all of the sample types (Fig. 2), and the magnitudes varied systematically with the autocorrelation order and the sample type (Fig. 3). In many cases, the magnitudes were high enough so that correlation distances could also be estimated (Fig. 4).

A model in which the surfaces were assumed to be populated by discrete regions with different concentrations of fluorescent molecules (and therefore different fluorescence intensities) was developed. Analysis of the autocorrelation function magnitudes with this model gave results (Table I) that were qualitatively consistent with visual inspection of the images. The results of analysis with this model were also combined with the first-order correlation distances to estimate cluster densities; the densities were also consistent with visual impressions.

Receptor oligomerization has been implicated or confirmed in a large variety of signal transduction processes. However, few experimental methods exist for examining the oligomerization of cell surface receptors. It is apparent from the initial work presented here that high-order I-FCS can generate useful information about nonuniform spatial distributions of fluorescent molecules in planar membranes. Future development will include

application of high-order I-FCS to model and natural cell membranes containing proteins distributed among small oligomerization states (e.g., monomers and dimers).

APPENDIX: MODELS FOR SURFACE INHOMOGENEITIES

Equations (9) and (10) are a system of $s + 1$ equations which can be solved algebraically to give expressions for the a_{si} and b_{si} as a function of the B_p for $2 \leq p \leq s + 1$. The results, which are similar to equations previously derived in a different context [40], are as follows:

For one parameter (B_2), $s = 1$, $q = 2$, $b_{11} = 1$, $b_{12} = 0$, and

$$a_{11} = \frac{1}{B_2}, \qquad a_{12} = 1 - \frac{1}{B_2} \tag{A1}$$

For two parameters (B_2 and B_3), $s = 2$, $q = 2$, $b_{21} = 1$, and

$$z = \frac{(B_3 - B_2) \pm \sqrt{(B_3 - B_2)^2 + 4(B_3 - B_2^2)(1 - B_2)}}{2(B_3 - B_2^2)}$$

$$b_{22} = \frac{z(zB_2 - 1)}{z - 1}, \quad a_{22} = \frac{z - 1}{b_{22} - 1}, \quad a_{21} = 1 - a_{22} \tag{A2}$$

The first equation is solved for two values of z, and the z values are used in the second and third equations. The two z values give solutions for b_{22} which are reciprocals of each other, with a_{21} and a_{22} switched in assignment. Results are reported in the form for which $b_{22} > 1$.

For three parameters (B_2, B_3, and B_4), $s = 3$, $q = 3$, $b_{31} = 1$, $b_{33} = 0$, and

$$z = \frac{(B_4 - B_3B_2) \pm \sqrt{(B_4 - B_3B_2)^2 + 4(B_2^2 - B_3)(B_4B_2 - B_3^2)}}{2(B_4B_2 - B_3^2)}$$

$$b_{32} = \frac{z(zB_3 - B_2)}{zB_2 - 1}, \qquad a_{32} = \frac{z(zB_2 - 1)}{b_{32}(b_{32} - 1)} \tag{A3}$$

$$a_{31} = z - a_{32}b_{32}, \qquad a_3 = 1 - (a_{32} + a_{31})$$

The two z values give reciprocal solutions for b_{32}; the solution for which $b_{32} > 1$ is reported.

For four parameters (B_2, B_3, B_4, and B_5), $s = 4$, $q = 3$, $b_{41} = 1$, and

$$\begin{aligned}&[B_4^2 - B_5B_3 + B_3^3 - 2B_4B_3B_2 + B_5B_2^2]z^3\\ &+ [B_4B_3 - B_4^2 - B_3^2B_2 + B_4B_2^2 + B_5B_3 - B_5B_2]z^2\\ &+ [B_5 - B_3^2 - B_4B_2 + B_4B_3 - B_5B_2 + B_3B_2^2]z\\ &+ [B_4B_2 - B_3^2 - B_2^3 + 2B_3B_2 - B_4] = 0\end{aligned} \tag{A4}$$

$$\begin{aligned}\phi_1 &= [(zB_4 - B_3)(z - 1) - (zB_3 - B_2)(zB_2 - 1)]z\\ \phi_2 &= [(zB_4 - B_3)(zB_2 - 1) - (zB_3 - B_2)^2]z\\ \phi_3 &= (z - 1)(zB_3 - B_2) - (zB_2 - 1)^2\end{aligned} \tag{A5}$$

$$b_{42,43} = \frac{\phi_1 \pm \sqrt{\phi_1^2 - 4\phi_2\phi_3}}{2\phi_3}$$

$$a_{42,43} = \frac{z^2B_2 - (b_{43,42} + 1)z + b_{43,42}}{(b_{43,42} - b_{42,43})(1 - b_{42,43})} \tag{A6}$$

$$a_{41} = 1 - (a_{42} + a_{43})$$

The three z values were found numerically. These values of z, with the two solutions to the fifth equation, give six solutions corresponding to the six permutations in index assignment for the a_{4i}'s. Results are reported in the form where $a_{41} > a_{42} > a_{43}$. These assignments were made before averaging the results of individual images.

For five parameters (B_2, B_3, B_4, B_5, and B_6), $s = 5$, $q = 4$, $b_{51} = 1$, $b_{54} = 0$, and

$$\begin{aligned}&[B_6B_3^2 + B_4^3 + B_5^2B_2 - 2B_5B_4B_3 - B_6B_4B_2]z^3\\ &+ [B_5B_3^2 - B_4^2B_3 - B_5^2 + B_6B_4 - B_6B_3B_2 + B_5B_4B_2]z^2\\ &+ [B_6B_2^2 + B_4B_3^2 + B_5B_4 - B_4^2B_2 - B_5B_3B_2 - B_6B_3]z\\ &+ [2B_4B_3B_2 - B_5B_2^2 - B_4^2 - B_3^3 + B_5B_3] = 0\end{aligned} \tag{A7}$$

$$\begin{aligned}\phi_1 &= [(zB_4 - B_3)(zB_3 - B_2) - (zB_5 - B_4)(zB_2 - 1)]z\\ \phi_2 &= [(zB_4 - B_3)^2 - (zB_5 - B_4)(zB_3 - B_2)]z^2\\ \phi_3 &= (zB_3 - B_2)^2 - (zB_4 - B_3)(zB_2 - 1)\end{aligned} \tag{A8}$$

$$b_{52,53} = \frac{\phi_1 \pm \sqrt{\phi_1^2 - 4\phi_2\phi_3}}{2\phi_3}$$

$$a_{52,53} = \frac{[z^2B_3 - z(b_{53,52} + 1)B_2 + b_{53,52}]z}{b_{52,53}(b_{53,52} - b_{52,53})(1 - b_{52,53})}$$

$$a_{51} = z - (a_{52}b_{52} + a_{53}b_{53}) \tag{A9}$$

$$a_{54} = 1 - (a_{53} + a_{52} + a_{51})$$

Assignments were made as described above for the four-parameter model ($a_{51} > a_{52} > a_{53}$).

ACKNOWLEDGMENTS

We thank Zoya N. Volovyk for assistance in composing Figs. 3 and 4. This work was supported by NIH Grant GM-37145 and by NSF Grant DMB-9728116.

REFERENCES

1. J. Matko and M. Edidin (1997) *Methods Enzymol.* **278**, 444–462.
2. K. Kwiatkowska and A. Sobota (1999) *Bioessays* **21**, 422–431.
3. W. J. Fantl, D. E. Johnson, and L. T. Williams (1993) *Annu. Rev. Biochem.* **62**, 453–481.
4. C. H. Heldin (1995) *Cell* **80**, 213–223.
5. S. C. Froehner (1993) *Annu. Rev. Neurosci.* **16**, 347–368.
6. B. J. Bormann and D. M. Engelman (1992) *Annu. Rev. Biophys. Biomol. Struct.* **21**, 223–242.
7. M. Zhou, S. Felder, M. Rubinstein, D. R. Hurwitz, A. Ullrich, I. Lax, and J. Schlessinger (1993) *Biochemistry* **32**, 8193–8198.
8. B. C. Cunningham, M. Ultsch, A. M. de Vos, M. G. Mulkerrin, K. R. Caluser, and J. A. Wells (1991) *Science* **254**, 821–825.
9. H. S. Earp, T. L. Dawson, X. Li, and H. Yu (1995) *Breast Cancer Res. Treat.* **35**, 115–132.
10. J. M. Sherrill and J. Kyte (1996) *Biochemistry* **35**, 5705–5718.
11. M. W. Pantoliano, R. A. Horlick, B. A. Springer, D. E. Van Dyk, T. Tobery, D. R. Wetmore, J. D. Lear, A. T. Nahapetian, J. D. Bradley, and W. P. Sick (1994) *Biochemistry* **33**, 10229–10248.
12. T. Spivak-Kroizman, M. A. Lemmon, I. Dikic, J. E. Ladbury, D. Pinchasi, J. Huang, M. Jaye, G. Crumley, J. Schlessinger, and I. Lax (1994) *Cell* **79**, 1015–1024.
13. T. Horan, J. Wen, L. Nahri, V. Parker, A. Garcia, T. Arakawa, and I. Philo (1996) *Biochemistry* **35**, 4886–4896
14. A. Sette, J. Alexander, J. Ruppert, K. Snoke, A. Franco, G. Ishioka, and H. M. Grey (1994) *Annu. Rev. Immunol.* **12**, 413–431.
15. I. Tamir, R. Schweitzer-Stenner, and I. Pecht (1996) *Biochemistry* **35**, 6872–6883.
16. O. H. Choi, J. H. Kim, and J. P. Kinet (1996) *Nature* **380**, 634–636.
17. S. Miyamoto, S. K. Akiyama, and K. M. Yamada (1995) *Science* **267**, 883–885.
18. K. Yamada, E. Goncalves, J. L. Carpenter, C. R. Kahn, and S. E. Shoelson (1995) *Biochemistry* **34**, 946–954.
19. M. Murakami, M. Hibi, N. Nakagawa, T. Nagakawa. K. Yasukawa, K. Yamanishi, T. Taga, and T. Kishimoto (1993) *Science* **260**, 1808–1810.
20. J. S. Philo, K. H. Aoki, T. Arakawa, L. O. Narhi, and J. Wen (1996) *Biochemistry* **35**, 1681–1691
21. N. L. Thompson (1991) in J. R. Lakowicz (Ed.), *Topics in Fluorescence Spectroscopy* (Plenum Press, New York), Vol. 1, Chap. 6.
22. A. G. Palmer and N. L. Thompson (1989) *Proc. Natl. Acad. Sci. USA* **86**, 6148–6152.
23. A. G. Palmer and N. L. Thompson (1989) *Chem. Phys. Lipids* **50**, 253–270.
24. N. O. Petersen, D. C. Johnson, and M. J. Schlesinger (1986) *Biophys. J.* **49**, 817–820.
25. N. O. Petersen (1986) *Biophys. J.* **49**, 809–815.
26. T. Meyer and H. Schindler (1988) *Biophys. J.* **54**, 983–993.
27. P. R. St-Pierre and N. O. Petersen (1990) *Biophys. J.* **58**, 503–511.
28. P. R. St-Pierre and N. O. Petersen (1992) *Biochemistry* **31**, 2459–2463.
29. D. E. Kopppel, F. Morgan, A. E. Cowan and J. H. Carson (1994) *Biophys. J.* **66**, 502–507.
30. K. M. Berland, P. T. C. So, and E. Gratton (1995) *Biophys. J.* **68**, 694–701.
31. K. M. Berland, P. T. So, Y. Chen, W. W. Mantulin, and E. Gratton (1996) *Biophys. J.* **71**, 410–420.
32. N. O. Petersen, P. L. Hoddelius, P. W. Wiseman, O. Seger, and K.-E. Magnusson (1993) *Biophys. J.* **65**, 1135–1146.
33. M. D. Wang and D. Axelrod (1994) *Bioimaging* **2**, 22–35.
34. Z. Huang and N. L. Thompson (1996) *Biophys. J.* **70**, 2001–2007.
35. E. Fire, C. M. Brown, M. G. Roth, Y. I. Henis, and N. O. Petersen (1997) *J. Biol. Chem.* **272**, 29538–29545.
36. B. J. Rasmusson, T. D. Flanagan, S. J. Turco, R. M. Epand, and N. O. Petersen (1998) *Biochim. Biophys. Acta Mol. Cell. Res.* **1404**, 338–352.
37. C. M. Brown and N. O. Petersen (1998) *J. Cell Sci.* **111**, 271–281.
38. P. W. Wiseman and N. O. Petersen (1999) *Biophys. J.* **76**, 963–977.
39. U. Meseth, T. Wohland, R. Rigler, and H. Vogel (1999) *Biophys. J.* **76**, 1619–1631.
40. A. G. Palmer and N. L. Thompson (1987) *Biophys. J.* **52**, 257–270.
41. A. G. Palmer and N. L. Thompson (1989) *Rev. Sci. Instrum.* **60**, 624–633.
42. A. G. Palmer and N. L. Thompson (1989) *Appl. Opt.* **28**, 1214–1220.
43. H. Qian and E. L. Elson (1990) *Proc. Natl. Acad. Sci. USA* **87**, 5479–5483.
44. H. Qian and E. L. Elson (1990) *Biophys. J.* **57**, 375–380.
45. M. L. Pisarchick and N. L. Thompson (1990) *Biophys. J.* **58**, 1235–1249.
46. M. M. Timbs and N. L. Thompson (1990) *Biophys. J.* **58**, 413–428.
47. K. H. Pearce, R. G. Hiskey, and N. L. Thompson (1992) *Biochemistry* **31**, 5983–5995.
48. H. V. Hsieh, C. L. Poglitsh, and N. L. Thompson (1992) *Biochemistry* **31**, 11562–11566.